PAPER • OPEN ACCESS

Influence of Zr-doping on the structure and transport properties of rare earth high-entropy oxides

To cite this article: Mohana V Kante *et al* 2024 *J. Phys. Energy* **6** 035001

View the article online for updates and enhancements.

Journal of Physics: Energy

Influence of Zr-doping on the structure and transport properties of rare earth high-entropy oxides

Mohana V Kante[1], Ajai R Lakshmi Nilayam[1,2], Kosova Kreka[3], Horst Hahn[1,4], Subramshu S Bhattacharya[5], Leonardo Velasco[6], Albert Tarancón[3,7], Christian Kübel[1,2], Simon Schweidler[1,*] and Miriam Botros[1,*]

1   Institute of Nanotechnology, Karlsruhe Institute of Technology, Kaiserstraße 12, 76131 Karlsruhe, Germany
2   Karlsruhe Nano Micro Facility (KNMFi), Karlsruhe institute of Technology, Kaiserstraße 12, 76131 Karlsruhe, Germany
3   Department of Advanced Materials for Energy, Catalonia Institute for Energy Research-IREC, Barcelona, Spain
4   The University of Oklahoma, School of Sustainable Chemical, Biological and Materials Engineering, 100 E. Boyd St., Norman, OK 73019, United States of America
5   Department of Metallurgical and Materials Engineering, Indian Institute of Technology Madras, Chennai 600036, India
6   Universidad Nacional de Colombia sede de La Paz, Km 9 via Valledupar—La Paz, 202010 Cesar, Colombia
7   Catalan Institution for Research and Advanced Studies (ICREA), Barcelona, Spain
*   Authors to whom any correspondence should be addressed.

E-mail: simon.schweidler@kit.edu and miriam.botros@kit.edu

Abstract

Fluorite-type ceria-based ceramics are well established as oxygen ion conductors due to their high conductivity, superseding state-of-the-art electrolytes such as yttria-stabilized zirconia. However, at a specific temperature and oxygen partial pressure they occasionally exhibit electronic conduction attributed to polaron hopping via multivalent cations (e.g. Pr and Ce). $(Ce, La, Pr, Sm, Y)O_{2-\delta}$ is a high-entropy oxide with a fluorite-type structure, featuring low concentrations of multivalent cations that could potentially mitigate polaron hopping. However, $(Ce, La, Pr, Sm, Y)O_{2-\delta}$ undergoes a structural transition to the bixbyite-type structure above 1000 °C. In this study, we introduce Zr doping into $(Ce, La, Pr, Sm, Y)O_{2-\delta}$ to hinder the structural transition at elevated temperatures. Indeed, the fluorite structure at elevated temperatures is stabilized at approximately 10 at.% Zr doping. The total conductivity initially increases with doping, peaking at 5 at.% Zr doping, and subsequently decreases with further doping. Interestingly, electronic conductivity in $(Ce, La, Pr, Sm, Y)_{1-x}Zr_xO_{2-\delta}$ under oxidizing atmospheres is not significant and is lowest at 8 at.% Zr. These results suggest that ceria-based high-entropy oxides can serve as oxygen ion conductors with a significantly reduced electronic contribution. This work paves the way for new compositionally complex electrolytes as well as protective coatings for solid oxide fuel cells.

1. Introduction

An electrolyte exhibiting pure oxygen ion conduction is a vital component in a solid oxide fuel cell [1–4]. Ionic mobility in oxygen ion conductors relies on the migration of oxygen ions through oxygen vacancies and a suitable lattice structure facilitating ionic transport [1, 4]. However, the number of such structures is limited. Fluorite-type oxides are one such structure, where the cation typically has an oxidation state of $+4$ with a stoichiometry of MO_2. The introduction of a $+3$ cation creates oxygen vacancies, allowing ionic diffusion through the anionic lattice. Ceria is an example of such a fluorite-type oxide. Consequently, doped ceria-based oxides have been extensively investigated as oxygen ion conductors [5–16]. For oxygen ion conductors, it is essential to eliminate electronic conduction over a wide range of oxygen partial pressures to prevent short circuits in solid oxide cells. Ceria-based oxides are known to exhibit electronic conduction at various oxygen partial pressures in reducing atmospheres (10^{-30}–10^{-20} bar) as well as in oxidizing regions (10^{-5}–1 bar) [5, 8, 11, 16–20]. Pr-doped CeO_2 is an example that shows an electronic contribution in both oxidizing and reducing regimes due to the multiple valences of Ce and Pr [16, 18, 19, 21–23]. Electron

conduction in these systems occurs via polaron hopping between Pr^{3+}/Pr^{4+}, Ce^{3+}/Ce^{4+}, Pr^{3+}/Ce^{4+} and Ce^{3+}/Pr^{4+}. Changes in oxygen partial pressure influence the oxidation states of Ce and Pr, leading to corresponding alterations in conductivity. One potential approach to minimizing/avoiding polaron hopping between Ce and Pr is through decreasing the available hopping sites by decreasing the content of Ce and Pr. However, the fluorite structure is lost at Ce concentrations below 60 at.% of cations in traditional doped ceria and the fluorite structure transitions to other structures that might be less accommodating for oxygen ion mobility [24–28].

(Ce, La, Pr, Sm, Y)$O_{2-\delta}$ is a fluorite-type high-entropy oxide [29] in which the content of Ce, Pr is less than or equal to 40 at.% of cations while still maintaining the fluorite structure below 1000 °C. The low content of Ce and Pr can help reduce the available sites for polaron hopping, thereby reducing electronic conductivity. The remaining cations in (Ce, La, Pr, Sm, Y)$O_{2-\delta}$ are +3 cations leading to a high concentration of oxygen vacancies in the structure. As a result, at temperatures exceeding 1000 °C, (Ce, La, Pr, Sm, Y)$O_{2-\delta}$ undergoes an ordering of these oxygen vacancies and structurally transforms from fluorite to bixbyite [29–31]. In a recent high-throughput study by Kumbhakar *et al*, Zr^{4+} has been observed to stabilize the fluorite structure in rare earth high-entropy oxides [32]. However, there have been no detailed studies of the effect of Zr doping on the structure and electrochemical properties of Zr-doped (Ce, La, Pr, Sm, Y)$O_{2-\delta}$. In this work, the effects of Zr doping on the structure, oxidation state of Ce and Pr and conductivity of (Ce, La, Pr, Sm, Y)$O_{2-\delta}$ are investigated in detail, and the possibility of suppressing electronic conductivity in ceria-based high-entropy oxides is explored.

2. Experiment

Cerium oxide (CeO_2) (99.9%, abcr GmbH), lanthanum oxide (La_2O_3) (99.9%, abcr GmbH), praseodymium oxide (Pr_6O_{11}) (99.9%, abcr GmbH), samarium oxide (Sm_2O_3) (99.9%, abcr GmbH), yttrium oxide (Y_2O_3) (99.9%, abcr GmbH) and zirconium oxide (ZrO_2) (99%, Sigma-Aldrich) powders were used to synthesize the high-entropy oxides. The oxide powders in stoichiometric amounts were mixed and ball milled for 48 h (10 min run and 10 min break) at 500 rpm using a high-energy planetary ball mill (Retsch PM 200, Retsch GmbH). The weight ratio of ball to powder was 50:1. The powders obtained from ball milling were pressed into 8 mm pellets at 500 MPa and sintered at 1400 °C for 12 h in air; heating and cooling rates were set to 5 °C min^{-1}. $Y_{0.08}Zr_{0.92}O_2$ (8YSZ) pellets were prepared from commercially available 8YSZ powder (Neyco) following the same sintering parameters as the high-entropy oxides.

X-ray diffraction (XRD) was conducted on a Bruker D8 Advance diffractometer equipped with a Cu K$_\alpha$ x-ray source and super-speed LYNXEYE detector and a PANalytical Empyrean diffractometer. The XRD scan was done over a 2θ range of 10° to 90° with a step size of 0.02° for 3 and 11 s. Rietveld refinement was performed using FullProf® software. Imaging in a scanning electron microscope (SEM) was conducted using a Zeiss Leo 1530 electron microscope with a voltage of 3–5 kV and a working distance of 5 mm. Energy dispersive x-ray spectroscopy (EDS) in the SEM was performed at a voltage of 20 kV with a working distance of 7 mm. UV–Vis spectroscopy was done using a Cary 60 UV–Vis spectrometer (Agilent) equipped with a remote fiber optic diffuse reflectance accessory and Cary WinUV software. The baseline corrected spectra were collected between 1100 nm and 200 nm with a speed of 600 nm min^{-1}. The reflectance data were converted to absorbance (α) with the Kubelka–Munk function. Band gaps were extracted using the Tauc expression, which can be written as

$$(\alpha.h\nu)^{\frac{1}{\gamma}} = B\left(h\nu - E_g\right).$$

Here h is Planck's constant, ν is the photon frequency, E_g is the band gap of the material, B is a constant and γ is exponential factor that depends on the electronic transition where $\gamma = 1/2$ is for a direct band gap and $\gamma = 2$ for an indirect band gap [33]. Transmission electron microscopy (TEM) characterizations were carried out by directly dispersing powders from crushed pellets onto a standard lacey carbon gold grid. The samples were examined using a double aberration-corrected state-of-the-art ThermoFischer Themis Z HR-(S)TEM (operated at 300 kV), equipped with a Super-X energy dispersive x-ray detector and a Gatan GIF Continuum 970 HighRes + K3 IS camera. Selected area electron diffraction (SAED), EDS and electron energy loss spectroscopy (EELS) were conducted inside the TEM to characterize the materials. Silver electrodes were coated on the pellets by applying silver paste (TED PELLA, Inc., PELCO conductive silver paste). The coated pellets were heat treated at 750 °C for 2 h to ensure adhesion. The pellets were then electrochemically characterized using electrochemical impedance spectroscopy (EIS) on a Bio-Logic VSP potentiostat in a frequency range from 1 MHz to 0.1 Hz and an amplitude of 500 mV. The EIS measurements were conducted at temperatures ranging from 300 °C to 700 °C and under oxygen partial pressures of

5 mbar to 1 bar in a custom-made setup from Huber Scientific. EC-Lab software was used to analyze and fit the impedance spectra.
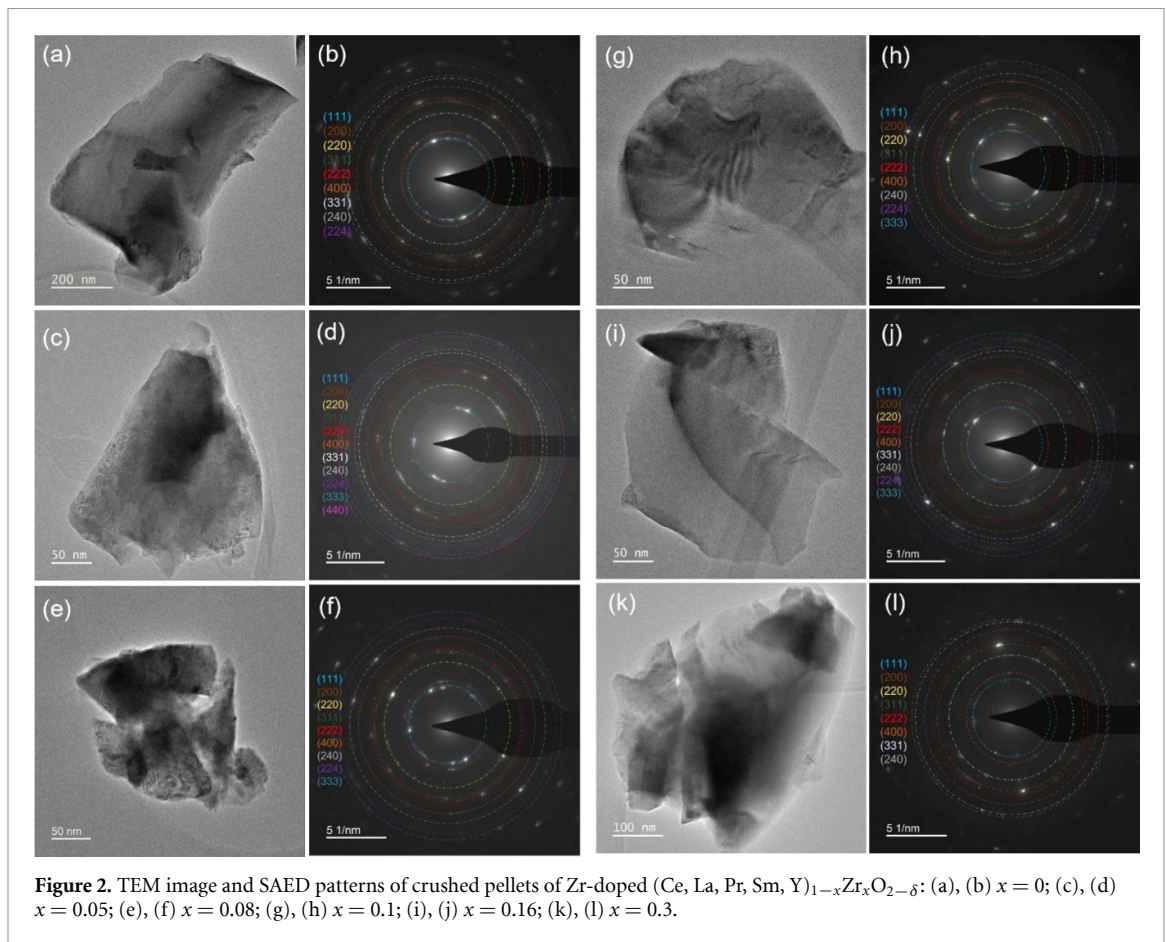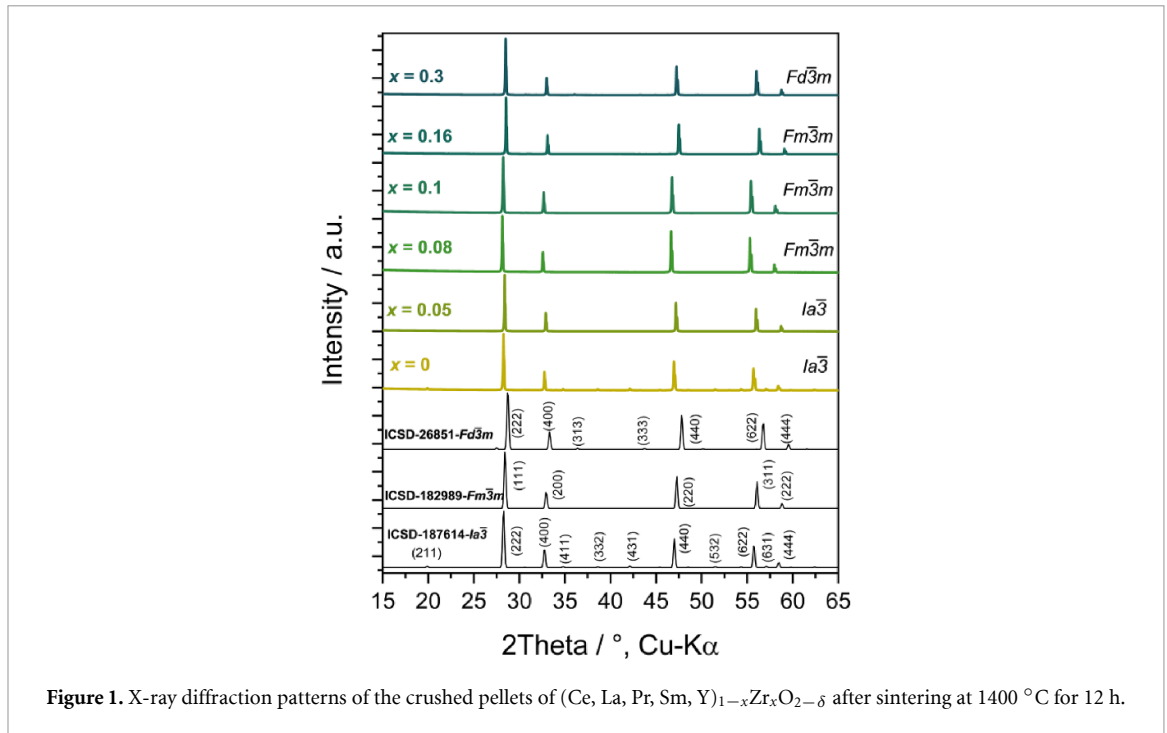
3. Results

The aim of this study is to investigate the influence of Zr doping on the structure, chemical homogeneity, oxidation states and electrochemical properties of $(Ce, La, Pr, Sm, Y)O_{2-\delta}$. The high-entropy materials were structurally characterized using XRD and TEM, chemically characterized with EDS, EELS and UV–Vis spectroscopy and electrochemically characterized by EIS at different temperatures and oxygen partial pressures.

3.1. Structural characterization

In order to analyze their crystal structure the sintered pellets were crushed to powders with a mortar and pestle and then investigated using XRD and TEM. The XRD patterns of the crushed pellets along with standard XRD patterns of the observed phases are displayed in figure 1. The XRD patterns of the as-prepared ball-milled powders can be seen in figure S1(a) along with the XRD patterns measured on the surface of the pellets in figure S1(b). XRD patterns of the pellets (both crushed pellets and the pellet surfaces) with different amounts of Zr suggest a transition from a bixbyite ($Ia\bar{3}$) phase for $x = 0, 0.05$ to a fluorite phase for $x = 0.08, 0.10$ and 0.16. A higher Zr content of $x = 0.3$ resulted in a pyrochlore-type ($Fd\bar{3}m$) structure. Rietveld refinement was performed on XRD patterns with the aforementioned structures to match the corresponding compositions, and the fits can be seen in figure S2. The XRD data suggest that all compositions are single phases.

The SAED patterns from TEM can be seen in figure 2. The indexed diffraction patterns of $x = 0$ and 0.05 in figures 2(b) and (d) show a fluorite structure, whereas the XRD pattern confirms the presence of the bixbyite phase. The bixbyite phase is also identified by SAED and is shown in the supplementary information (figure S3(a)). Likewise, the SAED pattern for $x = 0.08$ shows a bixbyite structure, contrary to the fluorite structure observed in the XRD pattern from figure 1. Thus, a phase mixture of fluorite and bixbyite is observed for 0 at.%, 5 at.% and 8 at.% Zr. In fluorite-structured oxides doped with higher concentrations of $+3$ cations, the oxygen vacancies tend to order near the dopant cations [2, 12, 34–37]. This results in the formation of bixbyite structure domains adjacent to the dopant cations. As the concentration of $+3$ cations increases, the size of these domains expands, eventually leading to a structural transition to bixbyite at high dopant concentrations. As a result, at a certain dopant concentration the presence of both fluorite and bixbyite has been observed in Y-, Gd-, La-, Yb- and Lu-doped ceria [38–43]. In several studies, the presence of a two-phase mixture could not be identified by XRD and could only be identified using advanced characterization techniques such as SAED/TEM and neutron diffraction [38–40]. The difference in XRD patterns of fluorite and bixbyite are small superstructure reflections present for the bixbyite structure, which can be seen in the XRD patterns from the ICSD database in figure 1. The diffraction pattern of the fluorite-type phase and bixbyite-type phase ($x = 0$) are otherwise identical when heat treated at the same temperature, according to a previous study [31]. As a result, we would like to note at this point that distinguishing between the different structures and probing the percentages of fluorite and bixbyite using XRD is not a straightforward process due to the similarities in the XRD patterns of the structures. However, any changes in the local structural ordering can be probed locally by electron diffraction in a TEM, as observed in this study. For $x = 0.1$ and $x = 0.16$, the diffraction spots are characteristic of the fluorite structure and are single phases. The SAED pattern for $x = 0.3$ shows a combination of fluorite (figure 2(i)) and pyrochlore (figure S2 (c)) characteristics, suggesting a biphasic mixture in $x = 0.3$ as well. The unit cell of the fluorite structure comprises four cations and eight anions, with a stoichiometry of MO_2. In a fluorite-type oxide, the effective oxidation state of the cation should be $+4$ and the presence of $+3$ cations leads to the formation of oxygen vacancies. In $(Ce, La, Pr, Sm, Y)O_{2-\delta}$, only Ce and Pr exhibit $+4$ while the other cations are in the $+3$ state, resulting in a high oxygen vacancy concentration. Consequently, at higher temperatures, oxygen vacancies become ordered and the structure undergoes a transition to bixbyite characterized by a stoichiometry of M_2O_3. The stabilization of the fluorite structure for $x = 0.1$ and $x = 0.16$ even after sintering at 1400 °C is a result of the introduction of Zr, providing enough $+4$ cations to retain the fluorite structure. However, further addition of Zr leads to a structural transition to a pyrochlore-type phase ($M_2Zr_2O_7$) ($Fd\bar{3}m$) at $x = 0.3$. The pyrochlore structure is a derivative of the fluorite structure, wherein $+3$ and $+4$ cations are ordered along the (110) direction [44]. The Zr contents of these systems considered here are as per the values utilized for synthesis. Therefore, it is important to explore the actual concentrations and the chemical homogeneity of these compositionally complex materials by chemical characterization techniques.

Figure 1. X-ray diffraction patterns of the crushed pellets of $(Ce, La, Pr, Sm, Y)_{1-x}Zr_xO_{2-\delta}$ after sintering at 1400 °C for 12 h.

Figure 2. TEM image and SAED patterns of crushed pellets of Zr-doped $(Ce, La, Pr, Sm, Y)_{1-x}Zr_xO_{2-\delta}$: (a), (b) $x = 0$; (c), (d) $x = 0.05$; (e), (f) $x = 0.08$; (g), (h) $x = 0.1$; (i), (j) $x = 0.16$; (k), (l) $x = 0.3$.

3.2. Chemical characterization

The chemical composition of $(Ce, La, Pr, Sm, Y)_{1-x}Zr_xO_{2-\delta}$ compared with the Zr content (x) extracted from EDS data from SEM and TEM is shown in figure 3. It can be seen that the Zr content is higher (around 1–2 at.% deviation) than the initially assumed percentages during the synthesis. The chemical composition of the samples obtained with SEM at a micrometer scale is close to the chemical composition assumed during
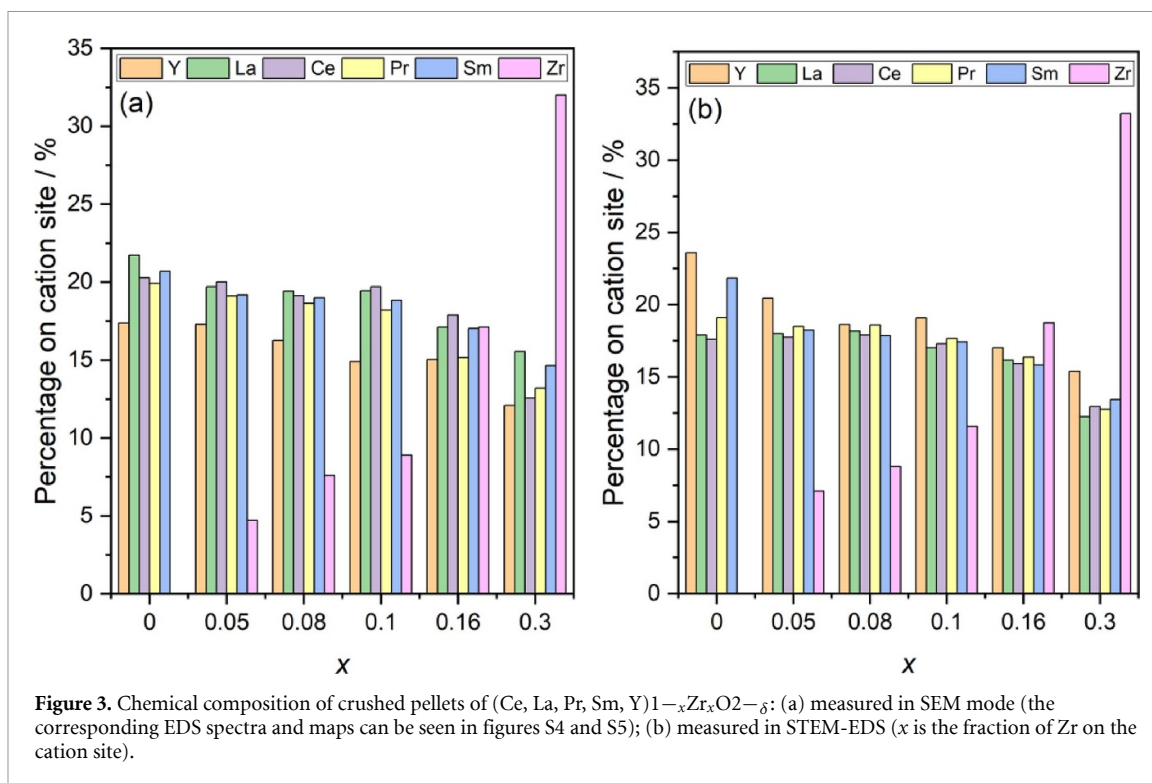
Figure 3. Chemical composition of crushed pellets of (Ce, La, Pr, Sm, Y)$1-x$Zr$_x$O2$-\delta$: (a) measured in SEM mode (the corresponding EDS spectra and maps can be seen in figures S4 and S5); (b) measured in STEM-EDS (x is the fraction of Zr on the cation site).

synthesis, as seen in figure 3(a). The chemical composition at nanoscale obtained by STEM-EDS is shown in figure 3(b). A slight variation in chemical composition at nanoscale of the particles from the crushed pellet is observed when compared with the chemical composition from SEM. These small compositional variations might affect the local structure, as the formation of a fluorite-type structure is affected by the concentration of +4 cations resulting in the coexistence of structures observed from the SAED patterns. The EDS maps are shown in figures 4 and S6. All constituent elements show a homogeneous distribution over the entire material at the respective scale, without any segregation or clustering of single elements.

It is important to determine the oxidation states of Ce and Pr as their multivalency has been observed to aid electronic conductivity in ceria-based electrolytes. Therefore, EELS was performed to investigate the oxidation state of Ce and Pr (figure 5). The EELS edge of Ce can be seen in figure 5(a). Ce exhibits an M_5 edge at approximately 882 eV, and the edge is a result of the electron energy loss due to the transition of electrons from the 3d orbital. The position of the M edge and the intensity ratio between M_5 and M_4 are good indicators for comparing the oxidation states. The edge for Ce^{4+} is at higher energies than for Ce^{3+} and intensity ratio between M_5 and M_4 is 1–1.1 for Ce^{3+}, 0.7–0.8 for Ce^{4+} [45–47]. In this study, the peak positions and an intensity ratio of 0.8 are observed to be identical to those of ceria ($Ce^{4+}O_2$), as seen in figure 5(a). It can be concluded that the oxidation state of Ce in all samples is +4. The M_5 edge of Pr is around 930 eV and the M_4 edge is around 945 eV, which originates from the transition of electrons from the 3d orbital of Pr. The integral intensity ratios between M_5 and M_4 peak (I_{M5}/I_{M4}) change from 1.3 to 1.4 with Zr content, further suggesting a decrease in the oxidation state of Pr. The presence of Pr^{3+} is supported by the fact that a shoulder has been observed for the M_4 edge, characteristic of Pr^{3+} [31, 48]. Also, the peak positions of all the samples in this study occur at a lower energy loss ($M_5 \sim$931.1 eV and $M_4 \sim$950.7 eV) compared with the peak positions of Pr_6O_{11} ($Pr^{3.66+}$, Pr^{4+}–66%, Pr^{3+}–33%; M_5 at 933.4 eV and M_4 at 953 eV) and the M_5/ M_4 intensity ratio is 1.3 to 1.4 for increasing concentrations of Zr compared with the intensity ratio of 1.1 in Pr_6O_{11}. In $Pr(PO_4)$, as a reference for pure Pr^{3+}, the M_5 and M_4 peak positions are at $\sim$930 eV and $\sim$949 eV, respectively, and the intensity ratio is around 1.8 [49]. A linear interpolation (figure S8) results in an average oxidation state around $Pr^{3.35+}$ (Pr^{4+}–35%, Pr^{3+}–65%) and $Pr^{3.55+}$ (Pr^{4+}–55%, Pr^{3+}–45%) and independent of Zr doping.

Another way to verify the multivalence of Pr is with the help of UV–Vis spectroscopy, as the multivalence of Pr can significantly influence the band gap of these materials [29, 30, 50]. UV–Vis spectroscopy was performed for these oxides to determine the optical band gap, and the corresponding spectra are presented in figure S9. The absorption coefficient (α) is calculated from the reflectance using the Kubelka–Munk function. The direct band gap is considered in the literature for ceria-based systems [29, 31]. As a result, Tauc
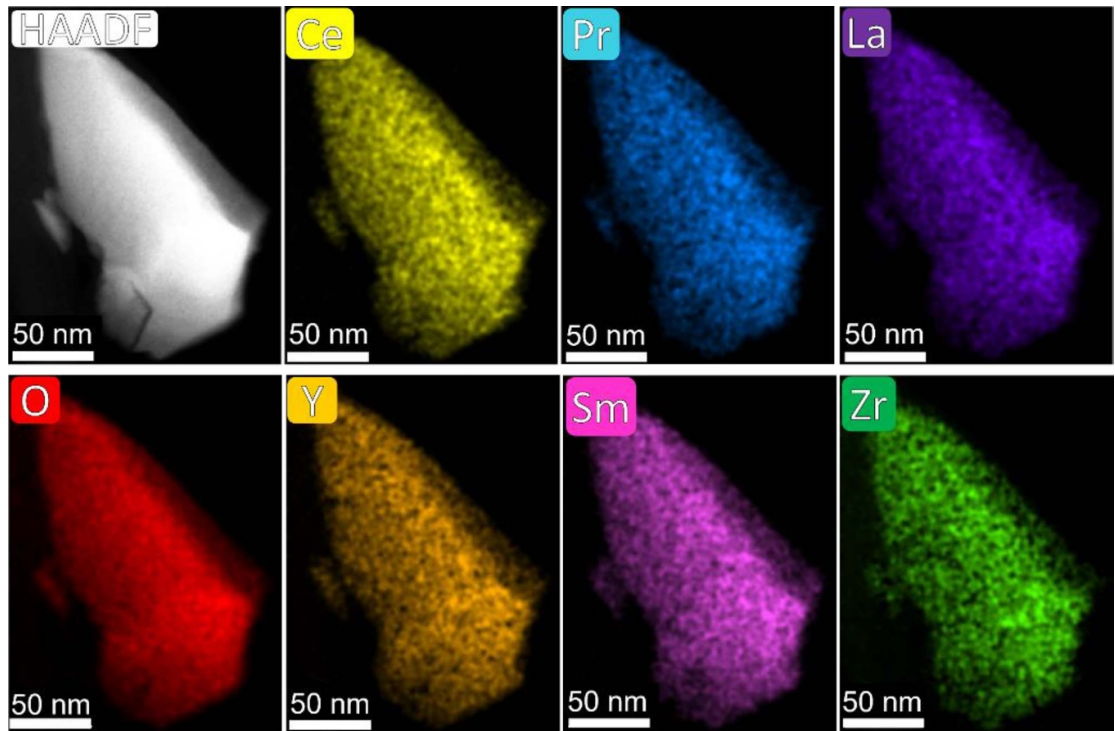
Figure 4. STEM-EDS mapping of the powders of crushed pellets of $(Ce, La, Pr, Sm, Y)_{0.92}Zr_{0.08}O_{2-\delta}$. The rest of the STEM-EDS maps of $(Ce, La, Pr, Sm, Y)1-_xZr_xO_{2-\delta}$ and corresponding EDS spectra can be in figure S7.
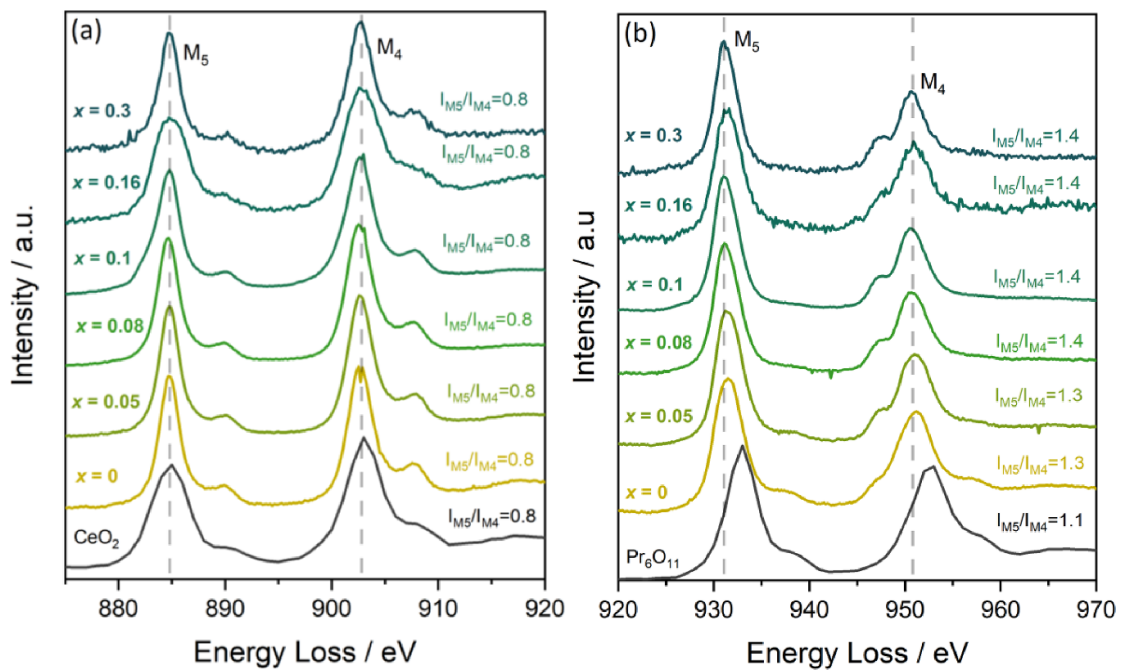

Figure 5. Electron energy loss spectroscopy of (a) the Ce edge and (b) the Pr edge of $(Ce, La, Pr, Sm, Y)_{1-x}Zr_xO_{2-\delta}$. Here the EELS data for CeO_2 and Pr_6O_{11} are taken from EELS.info.

plots ($(\alpha h\nu)^2$ versus $h\nu$) were generated for direct band gaps using data derived from UV–Vis spectra [33]. The Tauc plots can be seen in figure 6. According to the literature, the band gap of $(Ce, La, Pr, Sm, Y)O_{2-\delta}$ undergoes changes with variations in Pr^{4+} content, and the presence of Pr^{+4} is known to decrease the band gap from 3.2 to <2 eV [29, 31]. Notably, all the samples in this study show a band gap of less than 2 eV, providing clear evidence of the multivalence of Pr.
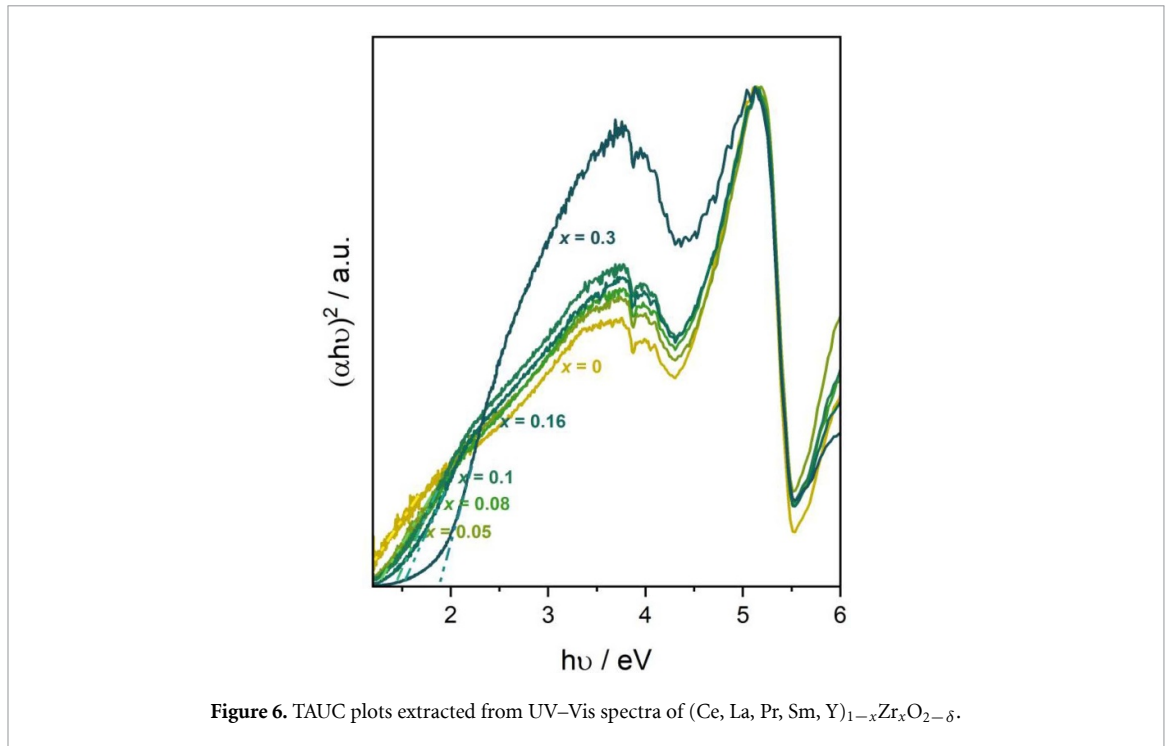
Figure 6. TAUC plots extracted from UV–Vis spectra of $(Ce, La, Pr, Sm, Y)_{1-x}Zr_xO_{2-\delta}$.

3.3. Conductivity studies

A dense pellet is required in order to measure the conduction behavior of these high-entropy oxides. The SEM of the surface and the cross section in figures S10 and S11 show dense pellets with indications of minor closed porosity. The relative densities calculated by the Archimedes method are between 90% and 95% of theoretical density (TD) and geometric relative densities are 85%–90% TD. The relative densities and SEM micrographs suggest that the pellets are suitable for oxygen ion mobility and conductivity measurements. The grain size of the pellets is observed to increase with increasing Zr content, reaching a maximum grain size at around 10 at.% Zr, and decreases with a further increase in Zr.

EIS measurements were made on pellets of $(Ce, La, Pr, Sm, Y)_{1-x}Zr_xO_{2-\delta}$ at different temperatures (300 °C–700 °C) and oxygen partial pressures from 5 mbar to 1 bar (figure 7). The Nyquist plots of the impedance data reveal the presence of two distinct semicircles: a large semicircle ranging from high to intermediate frequencies and a smaller semicircle at very low frequencies. To model this behavior, a two-element equivalent circuit with two (CPE // R) elements in series was employed. Each CPE // R circuit represents the impedance variations occurring in the electrolyte and the silver electrode, respectively. The impedance data were fitted with these two elements, and the resulting resistance and capacitance values can be seen in table S1. The capacitance and resistance values of the second element indicate its association with the electrode contribution [51, 52, 52]. The origin of the first semicircle is attributed to the oxide pellet. With increasing temperature, the conductivity increases and the impedance spectra become less detailed. At 600 °C, only a very small part of the first semicircle is visible, posing challenges for the precision of data fitting. The changes in the semicircle at high frequencies are not significant for different oxygen partial pressures at a given temperature. Consequently, a transition is made to comprehensive consideration of total conductivity for analytical purposes.

The total conductivities at different temperatures are plotted in the Arrhenius representation in figure 8(a) with the help of the following expression:

$$\sigma\left(T\right) = \frac{\sigma_0}{T}\exp\left(-\frac{E_A}{k_BT}\right) \tag{1}$$

Here, σ_0 is the pre-factor of the Arrhenius equation and E_A is the activation energy required for the hopping of charge carriers. The activation energies of $(Ce, La, Pr, Sm, Y)_{1-x}Zr_xO_{2-\delta}$ calculated from a linear fit of the experimental data in figure 8(a) range between 0.63 and 0.71 eV. The dependence of conductivity on the Zr content and temperature is shown in figure 8(b). The conductivity initially increases with increasing Zr content and reaches a maximum around $x = 0.05$; it then decreases on further addition of Zr. The decrease in conductivity is a consequence of the local ordering of oxygen vacancies and dopants [2, 12, 35–37]. In oxygen ion conductors, doping initially enhances conductivity, reaching a maximum at specific

Figure 7. Impedance spectra of $(Ce, La, Pr, Sm, Y)_{0.95}Zr_{0.05}O_{2-\delta}$ at (a) 300 °C, (b) 400 °C and (c) 600 °C.
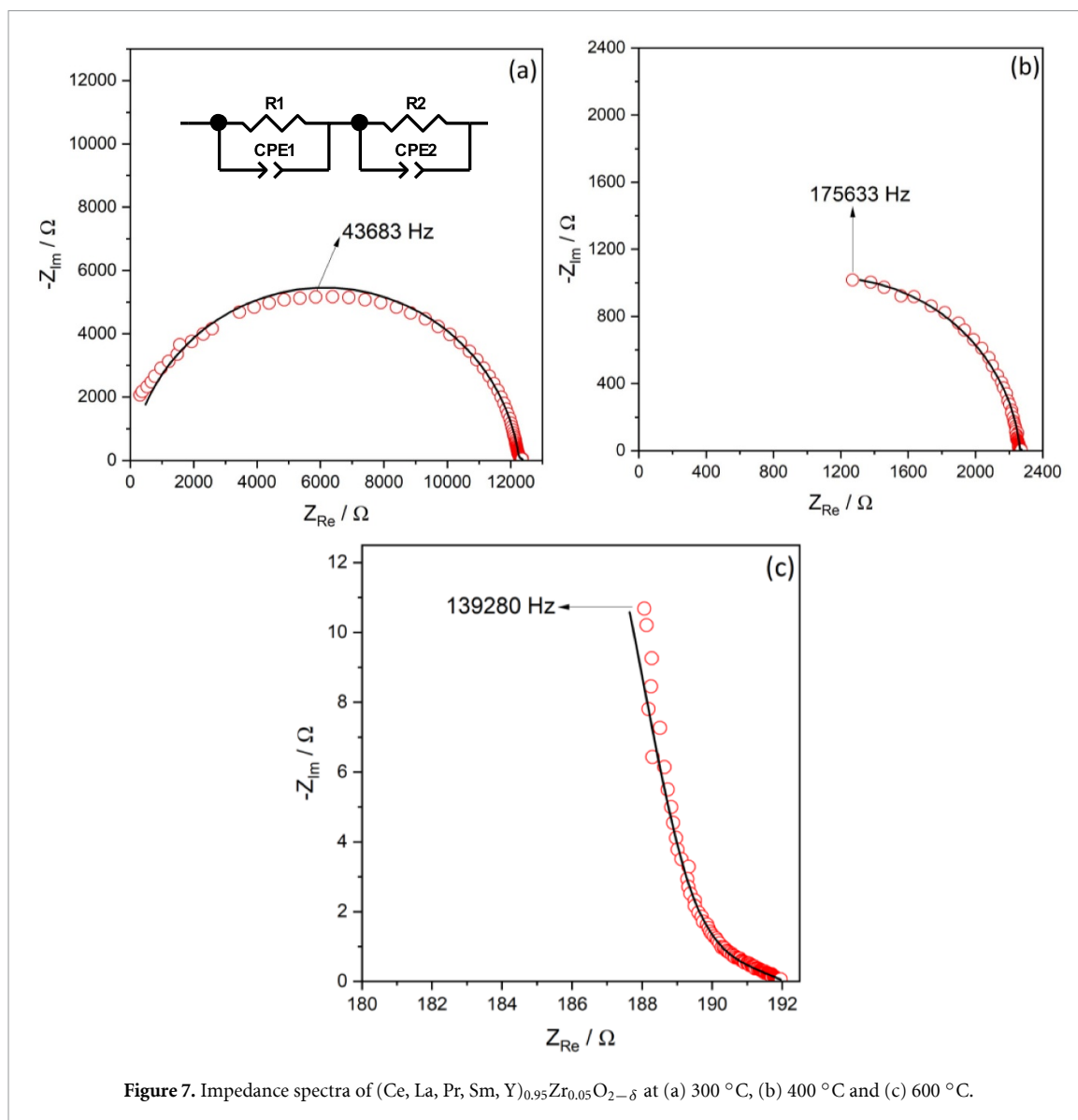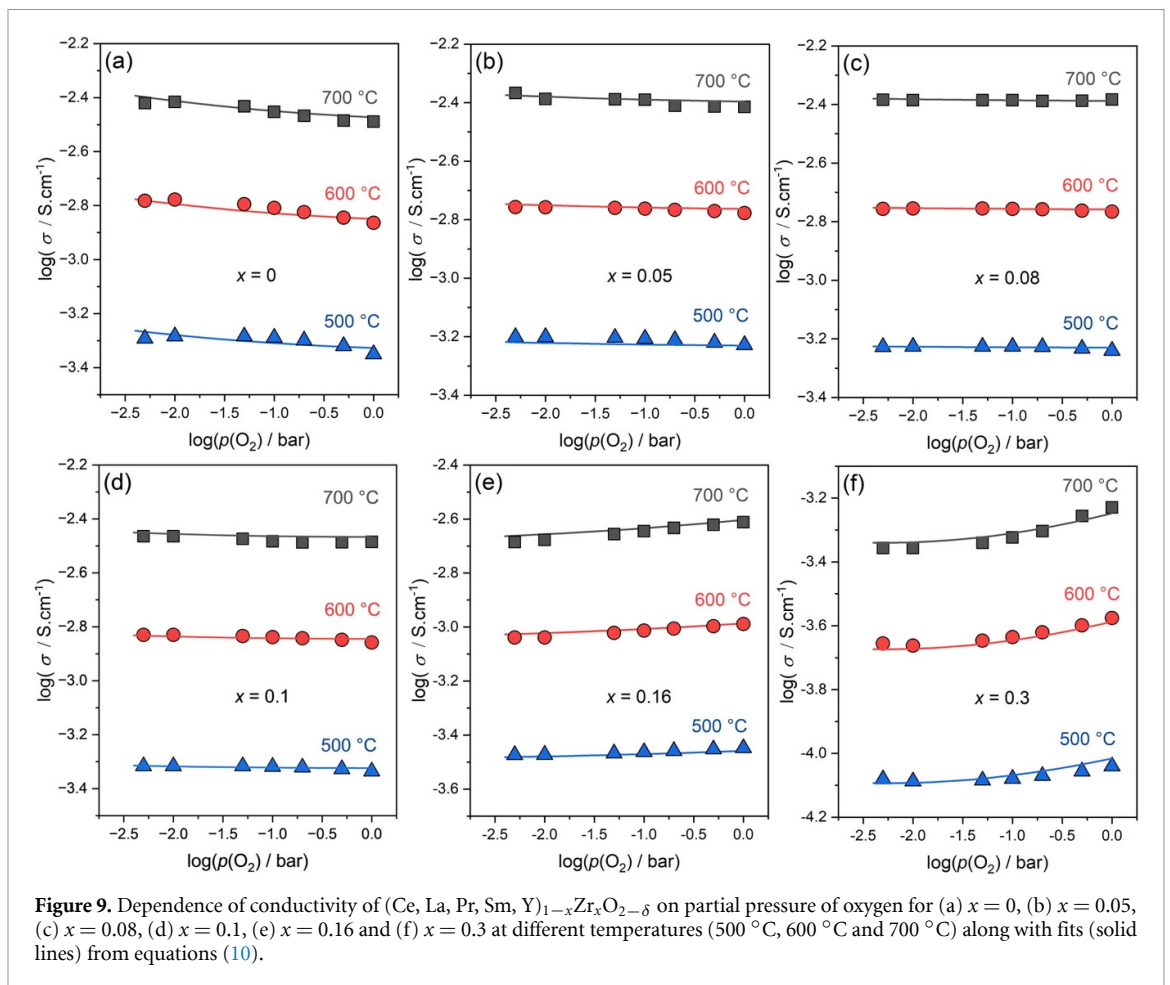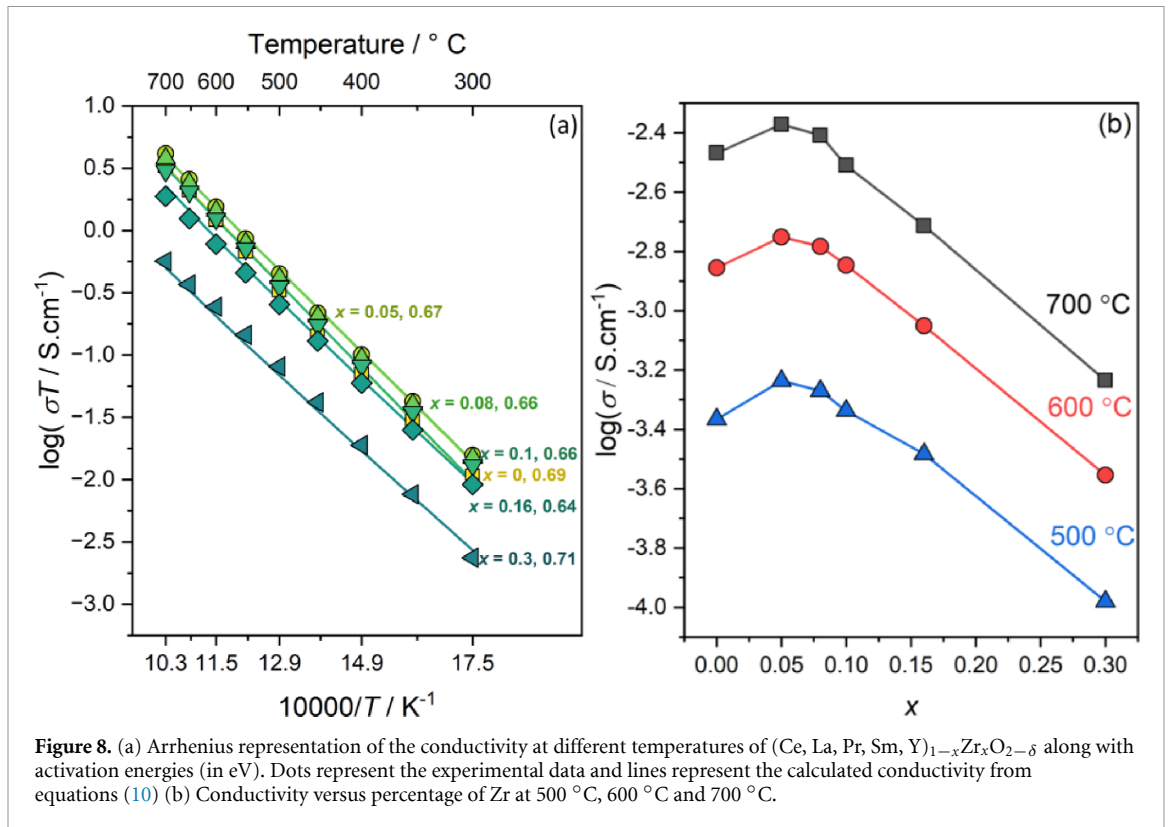
doping concentrations. However, beyond this optimal point, further doping results in a decline in conductivity [2, 12, 34–37]. It is postulated that high amounts of doping lead to a decrease in conductivity due to defect interactions. It should be noted that the small grain size at high Zr content seen in supplementary figures S10 and S11 could be another factor that leads to the lower conductivity observed for $x = 0.16$ and $x = 0.3$. The ions in ionic conductors are 'blocked' at the grain boundaries due to the higher activation energy, leading to lower conductivities in systems with smaller grain sizes [53].

The dependence of the conductivity on oxygen partial pressure was measured at different temperatures and can be seen in figure 9. All the samples show minimal alterations in conductivity in response to varying oxygen partial pressure. The slope of the conductivity plotted against p_{O_2} for all the samples is below 1/12. The small slopes indicate a very low electronic contribution and that the conductivity is predominantly ionic.

3.4. Effect of Pr multivalency on conductivity

The electronic conductivity in this system originates from multivalent Ce and Pr, while both Ce and Pr can change their oxidation with oxygen partial pressure. EELS data suggest that Ce exists in the +4 state and the transition of Ce^{4+} to Ce^{3+} can occur in reducing atmospheres (10^{-30}–10^{-20} bar) [5, 8, 11, 14, 16]. In this study, we explored the oxidizing regime (10^{-3}–1 bar) where changes in the oxidation state of Ce are non-existent. Consequently, the changes in conductivity due to Ce are not considered in this study. However, Pr changes its oxidation state in the measured oxidizing regime and several studies have observed a change in conductivity with oxygen partial pressure in Pr-doped ceria systems [16, 18, 19, 21, 22].

Figure 8. (a) Arrhenius representation of the conductivity at different temperatures of $(Ce, La, Pr, Sm, Y)_{1-x}Zr_xO_{2-\delta}$ along with activation energies (in eV). Dots represent the experimental data and lines represent the calculated conductivity from equations (10) (b) Conductivity versus percentage of Zr at 500 °C, 600 °C and 700 °C.

Figure 9. Dependence of conductivity of $(Ce, La, Pr, Sm, Y)_{1-x}Zr_xO_{2-\delta}$ on partial pressure of oxygen for (a) $x = 0$, (b) $x = 0.05$, (c) $x = 0.08$, (d) $x = 0.1$, (e) $x = 0.16$ and (f) $x = 0.3$ at different temperatures (500 °C, 600 °C and 700 °C) along with fits (solid lines) from equations (10).

In Pr-doped ceria, the following reaction corresponds to the change in oxidation state of Pr using Kroeger–Vink notation:

$$2Pr'_R + V_O^{\bullet\bullet} + \frac{1}{2}O_2 \rightleftharpoons 2Pr_R^\times + O_O^\times \,.$$
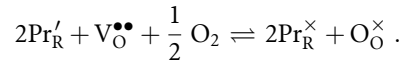
Here Pr'_R is Pr^{3+}, $V_O^{\bullet\bullet}$ is the oxygen vacancy, $Pr_R^\times$ is Pr^{4+} and $O_O^\times$ is lattice oxygen. The equilibrium constant for this reaction can be written as

$$K_1 = \frac{\left[Pr_R^\times\right]^2 \times \left[O_O^\times\right]}{\left[Pr'_R\right]^2 \times \left[V_O^{\bullet\bullet}\right] \times p(O_2)^{1/2}}. \tag{2}$$

The increase oxygen vacancy concentration in the structure is due to the introduction of $+3$ cations on the lattice, in the case of Pr-doped ceria, Pr^{3+}. As a result, the concentration of oxygen vacancies can be written as

$$\left[V_O^{\bullet\bullet}\right] = 2\left[Pr'_R\right]. \tag{3}$$

Substituting $\left[V_O^{\bullet\bullet}\right]$ from equation (3) to equation (2) along with further reiterating the equation along with the Brouwer approximation in which $Pr_R^\times$ and $O_O^\times$ can be considered constant gives the following expression:

$$\left[Pr'_R\right]^2 \times 2\left[Pr'_R\right] = \frac{\text{constant}}{K_1 \times p(O_2)^{1/2}} \tag{4}$$

$$\left[Pr'_R\right] \propto p(O_2)^{-\frac{1}{6}}. \tag{5}$$

The concentration of Pr^{3+} according to equation (5) is inversely proportional to $p(O_2)^{\frac{1}{6}}$. Polaron propagation happens via Pr^{3+}/Pr^{4+}. As a result, polaron propagation depends on the concentration of $\left[Pr'_R\right]$ with highest hopping occurring when $\left[Pr'_R\right] = 0.5$. Therefore, the conduction due to polaron hopping can be written as

$$\sigma_{\text{elec}} = e\left[Pr_R\right] m_{Pr}^{3+}\left(1 - m_{Pr}^{3+}\right)\frac{\mu_{\text{pol}}^0}{T}\exp\left(-\frac{\Delta H_{\text{mig}}}{k_B T}\right). \tag{6}$$

Here m_{Pr}^{3+} is the mole fraction of Pr^{3+} and ΔH_{mig} is the migration enthalpy for polaron hopping. According to equation (5), the concentration of Pr^{3+} changes with partial pressure of oxygen, which consequently changes the electronic conductivity with change in oxygen partial pressure. As a result, the electronic conductivity in Pr-doped ceria has been observed to exhibit n-type conduction with a partial pressure dependence of $p(O_2)^{-1/6}$ below 50% Pr^{3+} and p-type conduction with a partial pressure dependence of $p(O_2)^{1/6}$ above 50% Pr^{3+} [6, 7, 16, 18, 19, 21, 22]. The polaron conduction with respect to oxygen partial pressure can be written as

$$\text{when } m_{Pr}^{3+} < 0.5, \sigma_{\text{elec}}^n = \sigma_{\text{pol}}^n \times p(O_2)^{-\frac{1}{6}} = \frac{\sigma_o^{n-\text{pol}}}{T}\exp\left(-\frac{E_A^{\text{pol}}}{k_B T}\right)p(O_2)^{-\frac{1}{6}} \tag{7}$$

$$\text{when } m_{Pr}^{3+} > 0.5, \sigma_{\text{elec}}^p = \sigma_{\text{pol}}^p \times p(O_2)^{\frac{1}{6}} = \frac{\sigma_o^{p-\text{pol}}}{T}\exp\left(-\frac{E_A^{\text{pol}}}{k_B T}\right)p(O_2)^{\frac{1}{6}}. \tag{8}$$

Here σ_{elec}^n is the n-type electronic conduction observed when the Pr^{3+} content is lower than 50% and σ_{elec}^p is the p-type electronic conduction observed when the Pr^{3+} content is higher than 50%. σ_{pol}^n and σ_{pol}^p are the oxygen partial pressure-independent conductivities at a given temperature T for p-type and n-type conduction. The activation energy or the enthalpy of polaron migration are independent of the Pr^{3+} content but are rather dependent on the material system. Consequently, the activation energies for polaron migration (E_A^{pol}) for p-type and n-type conduction are considered to be the same for a given material system. However, the conductivity pre-factor is dependent on charge carrier concentration and not considered to be equal in

the fits. $\sigma_o^{n-\mathrm{pol}}$ and $\sigma_o^{p-\mathrm{pol}}$ are the conductivity pre-factors for n-type and p-type electronic conduction. The total conductivity of the material is the sum of the ionic and electronic conductivities of the system. Therefore, the total conductivity with respect to the partial pressure of oxygen can be written as

$$\sigma_{\mathrm{total}} = \sigma_{\mathrm{ion}} + \sigma_{\mathrm{elec}} = \sigma_{\mathrm{ion}} + \sigma_{\mathrm{elec}}^p + \sigma_{\mathrm{elec}}^n = \sigma_{\mathrm{ion}} + \sigma_{\mathrm{pol}}^n \times p(\mathrm{O}_2)^{-\frac{1}{6}} + \sigma_{\mathrm{pol}}^p \times p(\mathrm{O}_2)^{\frac{1}{6}}. \tag{9}$$

Here σ_{ion} is the ionic conductivity, and it is assumed to be independent of $p(\mathrm{O}_2)$ in a given partial pressure regime. Combining equation (7) or equation (8) with equation (9) and applying equation (1) to ionic conduction leads to the following:

$$\sigma_{\mathrm{total}} = \frac{\sigma_o^{\mathrm{ion}}}{T} \exp\left(-\frac{E_A^{\mathrm{ion}}}{k_B T}\right) + \frac{\sigma_o^{n-\mathrm{pol}}}{T} \exp\left(-\frac{E_A^{\mathrm{pol}}}{k_B T}\right) p(\mathrm{O}_2)^{-\frac{1}{6}} + \frac{\sigma_o^{p-\mathrm{pol}}}{T} \exp\left(-\frac{E_A^{\mathrm{pol}}}{k_B T}\right) p(\mathrm{O}_2)^{\frac{1}{6}}. \tag{10}$$

Here σ_o^{ion} is the conductivity pre-factor for ionic conductivity and E_A^{ion} is the activation energy for ion migration.

4. Discussion

In this study, compositions with $x = 0$, 0.05, 0.08 and 0.1 exhibit a negative slope for conductivity plotted against $p(\mathrm{O}_2)$, while for $x = 0.16$ and 0.3, a positive slope is observed (figure 9). The negative slope of conductivity plotted against $p(\mathrm{O}_2)$ for $x = 0$, 0.05, 0.08 and 0.1 indicates that $0.5 > m_{\mathrm{Pr}}^{3+}$. An increase in x_{Pr}^{3+} is observed with increasing Zr content and around $x = 0.16$ and 0.3, m_{Pr}^{3+} exceeds 0.5, resulting in the positive slope observed in figure 9. The conductivity versus $p(\mathrm{O}_2)$ suggests that the effective oxidation state of these oxides is around 3.5, which is in the range of linear interpolation of the EELS data in figure S5. The data from figure 9 for $x = 0$, 0.05, 0.08, 0.1, 0.16 and 0.3 are fitted with equation (10). The conductivity pre-factors and activation energies for ion and polaron migration are calculated from the fits and can be seen in table S2. The ionic conductivity (σ_{ion}) and the total electronic conduction (σ_{elec}) at 1 bar are calculated from the values in table S2. σ_{ion} and σ_{elec} were plotted in a bar graph with respect to the Zr content and can be seen in figure 10. The ionic conduction increases with increasing Zr content, reaches a maximum around $x = 0.08$ and decreases with further addition of Zr. The ionic conduction in various oxygen ion conductors is very well established to reach a maximum around 5–10 at.% doping concentration of the dopant [2, 12, 34]. Conversely, the pressure-independent electronic conduction decreases with increasing Zr content, reaches a minimum at $x = 0.10$ and increases with further addition of Zr. Even though $x = 0.1$ has the lowest electronic conductivity, its ionic conductivity is lower than for $x = 0.08$. As a result, $(\mathrm{Ce}, \mathrm{La}, \mathrm{Pr}, \mathrm{Sm}, \mathrm{Y})_{0.92}\mathrm{Zr}_{0.08}\mathrm{O}_{2-\delta}$ has the highest ionic conductivity as well as the highest transference number of the compositions investigated in this study as seen from the transference numbers in the supplementary information (figure S12).

$(\mathrm{Ce}, \mathrm{La}, \mathrm{Pr}, \mathrm{Sm}, \mathrm{Y})_{1-x}\mathrm{Zr}_x\mathrm{O}_{2-\delta}$ with Zr doping levels as low as 5 at.% shows a lower electronic character even in the presence of multivalent Pr, which has been observed to induce electronic partial conductivity in these systems [16, 18, 19, 22, 23]. In order for a polaron to propagate through Pr and Ce, there should be a Pr^{3+} adjacent to Pr^{4+} or Ce^{4+}. In a traditional oxide system such as Pr-doped CeO_2, a Pr^{3+} is surrounded by a Pr or Ce cation and the chance of finding Pr^{4+} and Ce^{4+} is higher, increasing the mobility of the electrons. However, in a multicomponent or high-entropy oxide such as $(\mathrm{Ce}, \mathrm{La}, \mathrm{Pr}, \mathrm{Sm}, \mathrm{Y})_{1-x}\mathrm{Zr}_x\mathrm{O}_{2-\delta}$, adjacent sites to a Pr^{3+} is shared by multiple elements (in this case Ce, Pr, Zr, La, Sm and Y; six elements). As a result, the probability of finding a Ce^{4+} or Pr^{4+} adjacent to Pr^{3+} is reduced and the mobility of the polaron decreases, leading to a lower electronic conductivity in the high-entropy oxide $(\mathrm{Ce}, \mathrm{La}, \mathrm{Pr}, \mathrm{Sm}, \mathrm{Y})_{1-x}\mathrm{Zr}_x\mathrm{O}_{2-\delta}$ when compared with Pr-doped ceria. However, an increase in electronic conductivity is observed for $x = 0.16$ and $x = 0.3$. The grain boundary contribution to the conductivity is not considered for $x = 0$, 0.05, 0.08 and 0.1 due to the large grain sizes ($> 2\ \mu\mathrm{m}$). Nevertheless, the grain size of $x = 0.16$ and $x = 0.3$ ($< 1\ \mu\mathrm{m}$) is smaller when compared with that of $x = 0$, 0.05, 0.08 and 0.1 and the mechanism of grain boundary conduction is unknown; it most likely will be different from that within the grain. The observed increase in electronic conductivity might be due to a grain boundary contribution, and further detailed impedance studies on samples with different grain sizes are necessary to understand the effect of grain boundaries on the conductivity. The temperature-dependent conductivity of $(\mathrm{Ce}, \mathrm{La}, \mathrm{Pr}, \mathrm{Sm}, \mathrm{Y})_{1-x}\mathrm{Zr}_x\mathrm{O}_{2-\delta}$ is compared with
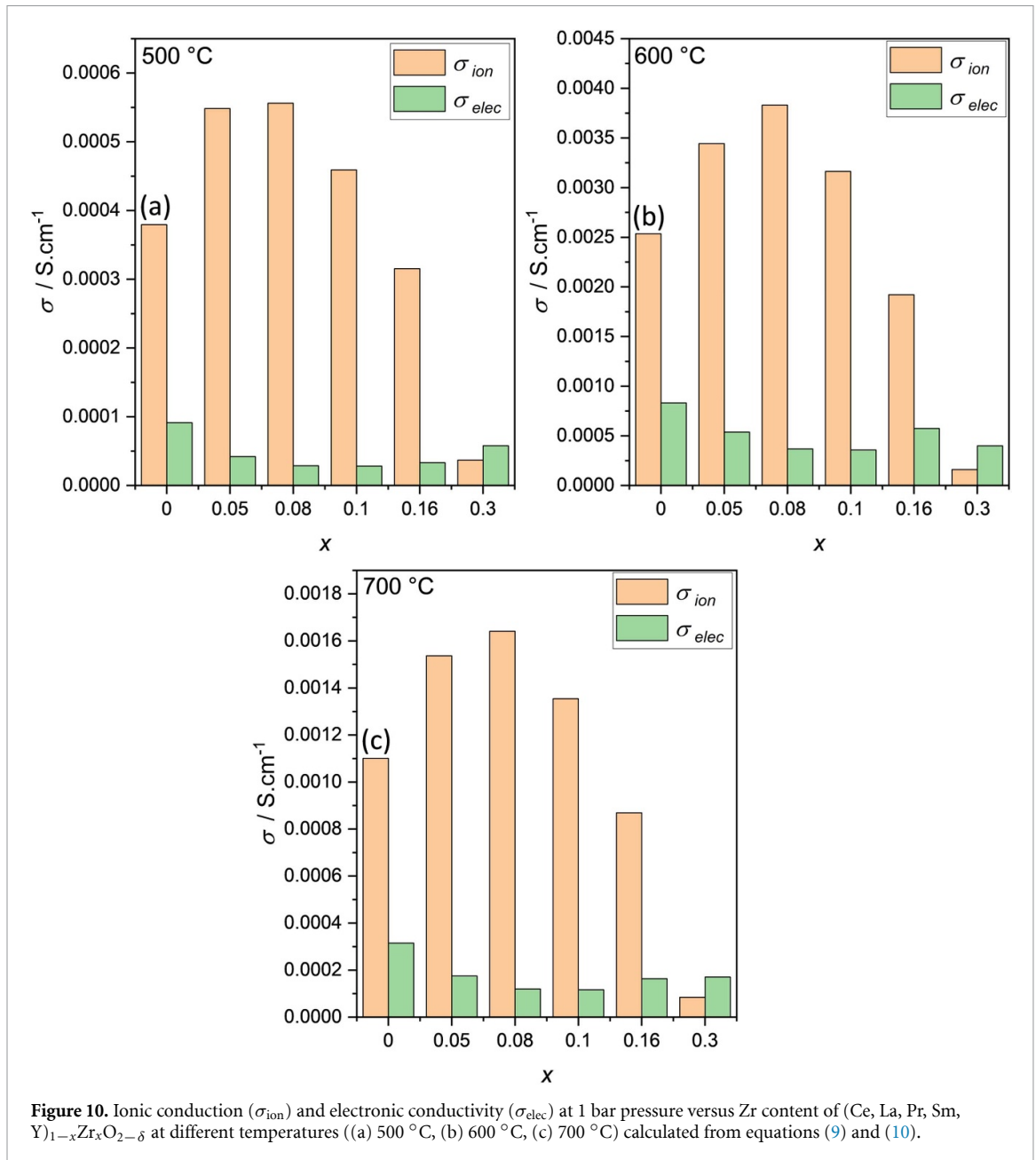
Figure 10. Ionic conduction (σ_{ion}) and electronic conductivity (σ_{elec}) at 1 bar pressure versus Zr content of (Ce, La, Pr, Sm, Y)$_{1-x}$Zr$_x$O$_{2-\delta}$ at different temperatures ((a) 500 °C, (b) 600 °C, (c) 700 °C) calculated from equations (9) and (10).

that of 8YSZ, and can be seen in figure 11. (Ce, La, Pr, Sm, Y)$_{1-x}$Zr$_x$O$_{2-\delta}$ exhibits higher conductivity than 8YSZ up to 600 °C after which 8YSZ has higher conductivity due to its larger activation energy. However, the conductivities are one to two orders of magnitude smaller than in ceria-based systems, bearing in mind that these systems are mixed ionic and electronic conductors [1–5, 7, 8, 11, 12, 16, 18–20]. In ceria-based systems, it is assumed that the ionic conductivity depends on the ionic size of the dopant [12]. The ionic size of the dopant should be close to the ionic radius of Ce^{4+}. The ionic radii of La^{3+} and Y^{3+} are significantly larger than that of Ce^{4+}. As a result, strategically replacing La and Y with better suited ions can help increase the ionic conduction in the material along with a decrease in the electronic contribution in high-entropy oxides due to the lack of polaron hopping sites. Finally, ceria-based high-entropy oxides show promise as oxygen ion conductors at low temperature ($<$500 °C) in solid oxide cells.

Figure 11. Comparison of $(Ce,La,Pr,Sm,Y)_{0.92}Zr_{0.08}O_{2-\delta}$ with 8YSZ in an Arrhenius representation.
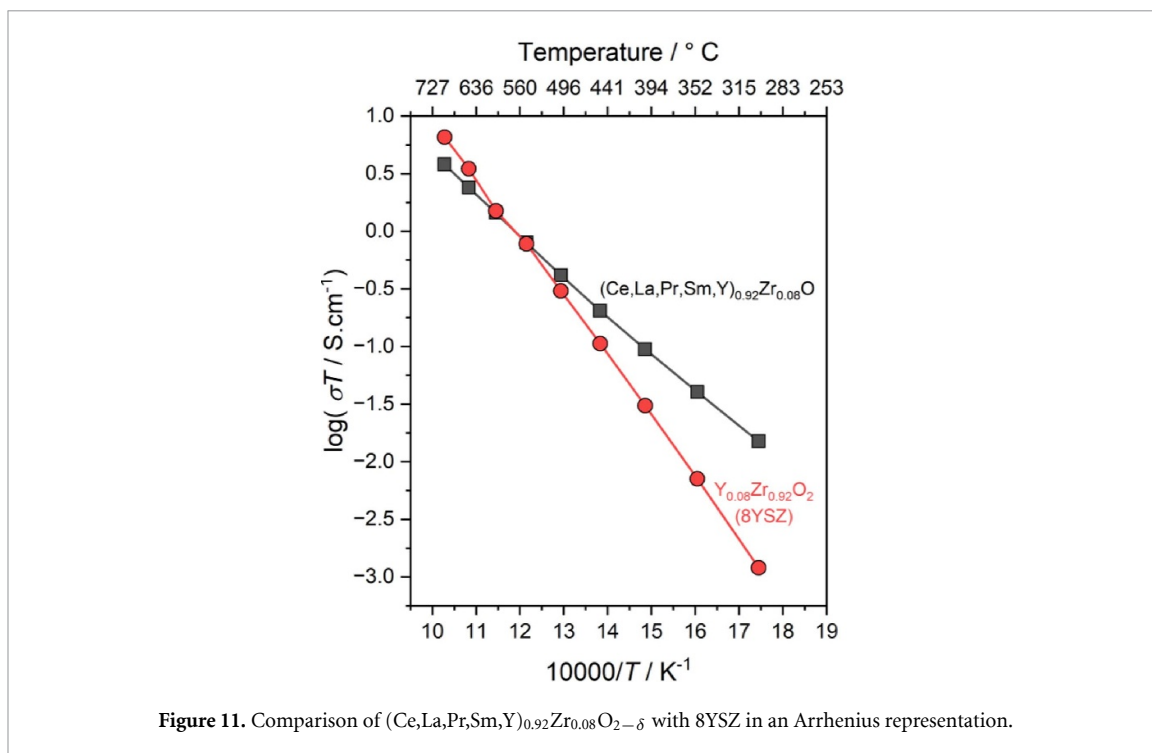
5. Conclusion

Stabilization of the fluorite-type structure was successfully achieved by incorporating Zr into (Ce, La, Pr, Sm, Y)$O_{2-\delta}$, which crystallizes in the bixbyite-type structure above 1000 °C. At an atomic percentage of 10 at.% Zr, the fluorite-type structure remained intact even at higher temperatures. A high amount of Zr (30 at.%) led to ordering of the Zr to form an additional pyrochlore-type structure. Pr is multivalent with, the Pr^{3+} content increasing with the Zr content. The conductivity increased initially, reached a maximum at $x = 0.05$ and decreased with further Zr doping. The dependence of the conductivity on oxygen partial pressure suggests that the systems investigated in this study had a dominant ionic contribution to the conductivity, with the highest values at $x = 0.08$. Despite the presence of multivalent Pr suggested by EELS and optical band gaps, the pressure dependence usually observed in Pr-doped ceria was not observed in (Ce, La, Pr, Sm, Y)$_{1-x}$Zr$_x$O$_{2-\delta}$ high-entropy oxides. As a result, the high-entropy oxides can be considered a potential solution to mitigate the electronic conductivity observed in doped ceria, while reaching ionic conductivities higher than 8YSZ at moderate temperatures.

Data availability statement

All data that support the findings of this study are included within the article (and any supplementary files). The TEM raw data set can be found under https://doi.org/10.35097/GcZKqFdyZsBbHMjv.

Acknowledgments

ORCID iDs

Kosova Kreka ● https://orcid.org/0000-0002-7864-2148
Albert Tarancón ● https://orcid.org/0000-0002-1933-2406
Miriam Botros ● https://orcid.org/0000-0003-1547-8149

References

[1] Fergus J W 2006 Electrolytes for solid oxide fuel cells *J. Power Sources* **162** 30–40
[2] Singhal S C and Kendall K 2003 *High-Temperature Solid Oxide Fuel Cells: Fundamentals, Design and Applications* (Elsevier) pp 1–405
[3] Jaiswal N, Tanwar K, Suman R, Kumar D, Uppadhya S and Parkash O 2019 A brief review on ceria based solid electrolytes for solid oxide fuel cells *J. Alloys Compd.* **781** 984–1005
[4] Skinner S J and Kilner J A 2003 Oxygen ion conductors *Mater. Today* **6** 30–37
[5] Navarro L, Marques F and Frade J 1997 n-Type conductivity in gadolinia-doped ceria *J. Electrochem. Soc.* **144** 267–73
[6] Bishop S R, Stefanik T S and Tuller H L 2012 Defects and transport in $Pr_xCe_{1-x}O_{2-\delta}$: composition trends *J. Mater. Res.* **27** 2009–16
[7] Chatzichristodoulou C, Park W S, Kim H S, Hendriksen P V and Yoo H I 2010 Experimental determination of the Onsager coefficients of transport for $Ce_{0.8}Pr_{0.2}O_{2-\delta}$ *Phys. Chem. Chem. Phys.* **12** 9637–49
[8] Wang S, Kobayashi T, Dokiya M and Hashimoto T 2000 Electrical and ionic conductivity of Gd-doped ceria *J. Electrochem. Soc.* **147** 3606
[9] Lai W and Haile S M 2005 Impedance spectroscopy as a tool for chemical and electrochemical analysis of mixed conductors: a case study of ceria *J. Am. Ceram. Soc.* **88** 2979–97
[10] Chueh W C, Lai W and Haile S M 2008 Electrochemical behavior of ceria with selected metal electrodes *Solid State Ion.* **179** 1036–41
[11] Gopal C B and Haile S M 2014 An electrical conductivity relaxation study of oxygen transport in samarium doped ceria *J. Mater. Chem. A* **2** 2405–17
[12] Li R, Koettgen J, Grieshammer S, Hein P, Grope B O H and Martin M 2018 Understanding the ionic conductivity maximum in doped ceria: trapping and blocking *Phys. Chem. Chem. Phys.* **20** 14291
[13] Celik E, Cop P, Negi R S, Mazilkin A, Ma Y, Klement P, Schörmann J, Chatterjee S, Brezesinski T and Elm M T 2022 Design of ordered mesoporous CeO_2-YSZ nanocomposite thin films with mixed ionic/electronic conductivity via surface engineering *ACS Nano* **16** 3182–93
[14] Celik E, Ma Y, Brezesinski T and Elm M T 2021 Ordered mesoporous metal oxides for electrochemical applications: correlation between structure, electrical properties and device performance *Phys. Chem. Chem. Phys.* **23** 10706–35
[15] Boaro M, Trovarelli A, Hwang J H and Mason T O 2002 Electrical and oxygen storage/release properties of nanocrystalline ceria–zirconia solid solutions *Solid State Ion.* **147** 85–95
[16] Michel K, Eufinger J P, Ulbrich G, Lerch M, Janek J and Elm M T 2017 Combining two redox active rare earth elements for oxygen storage—electrical properties and defect chemistry of ceria–praseodymia single crystals *Phys. Chem. Chem. Phys.* **19** 17661–9
[17] Tuller H L and Nowick A S 1977 Small polaron electron transport in reduced CeO_2 single crystals *J. Phys. Chem. Solids* **38** 859–67
[18] Bishop S R, Stefanik T S and Tuller H L 2011 Electrical conductivity and defect equilibria of $Pr_{0.1}Ce_{0.9}O_{2-\delta}$ *Phys. Chem. Chem. Phys.* **13** 10165–73
[19] Tuller H L, Bishop S R, Chen D, Kuru Y, Kim J J and Stefanik T S 2012 Praseodymium doped ceria: model mixed ionic electronic conductor with coupled electrical, optical, mechanical and chemical properties *Solid State Ion.* **225** 194–7
[20] Lee J H, Yoon S M, Kim B K, Kim J, Lee H W and Song H S 2001 Electrical conductivity and defect structure of yttria-doped ceria-stabilized zirconia *Solid State Ion.* **144** 175–84
[21] Nicollet C, Kalaev D and Tuller H L 2019 Mixed conductivity and oxygen surface exchange kinetics of lanthanum-praseodymium doped cerium dioxide *Solid State Ion.* **331** 96–101
[22] Stefanik T S 1973 Electrical properties and defect structures of praseodymium-cerium oxide solid solutions (available at: https://dspace.mit.edu/handle/1721.1/16623) (Accessed 19 October 2023)
[23] Harrington G F, Kalaev D, Yildiz B, Sasaki K, Perry N H and Tuller H L 2019 Tailoring nonstoichiometry and mixed ionic electronic conductivity in $Pr_{0.1}Ce_{0.9}O_{2-\delta}$/$SrTiO_3$ Heterostructures *ACS Appl. Mater. Interfaces* **11** 34841–53
[24] Belliè V, Joorst G, Stephan O, De Groot F M F and Weckhuysen B M 2006 Phase segregation in cerium-lanthanum solid solutions (available at: https://pubs.acs.org/sharingguidelines) (Accessed 22 October 2023)
[25] Kornienko O A, Sameljuk A V, Bykov O, Yurchenko Y V and Barshchevskaya A K 2020 Phase relation studies in the CeO_2–La_2O_3–Er_2O_3 system at 1500 °C *J. Eur. Ceram. Soc.* **40** 4184–90
[26] Ye T, Huang D and Wang Y 2021 Phase relationships of the CeO_2–Sm_2O_3 system at 1200 °C to 1600 °C in air *Ceram. Int.* **47** 9075–82
[27] Žguns P A, Ruban A V and Skorodumova N V 2018 Phase diagram and oxygen-vacancy ordering in the CeO_2–Gd_2O_3 system: a theoretical study *Phys. Chem. Chem. Phys.* **20** 11805–18
[28] Artini C, Pani M, Carnasciali M M, Plaisier J R and Costa G A 2016 Lu-, Sm-, and Gd-doped ceria: a comparative approach to their structural properties *Inorg. Chem.* **55** 10567–79
[29] Sarkar A, Loho C, Velasco L, Thomas T, Bhattacharya S S, Hahn H and Djenadic R 2017 Multicomponent equiatomic rare earth oxides with a narrow band gap and associated praseodymium multivalency *Dalton Trans.* **46** 12167–76
[30] Djenadic R, Sarkar A, Clemens O, Loho C, Botros M, Chakravadhanula V S K, Kübel C, Bhattacharya S S, Gandhi A S and Hahn H 2017 Multicomponent equiatomic rare earth oxides *Mater. Res. Lett.* **5** 102–9
[31] Sarkar A *et al* 2020 Role of intermediate 4f states in tuning the band structure of high entropy oxides *APL Mater.* **8** 051111
[32] Kumbhakar M *et al* 2023 High-throughput screening of high-entropy fluorite-type oxides as potential candidates for photovoltaic applications *Adv. Energy Mater.* **13** 2204337
[33] Makuła P, Pacia M and Macyk W 2018 How to correctly determine the band gap energy of modified semiconductor photocatalysts based on UV–vis spectra *J. Phys. Chem. Lett.* **9** 6814–7
[34] Ahamer C, Opitz A K, Rupp G M and Fleig J 2017 Revisiting the temperature dependent ionic conductivity of yttria stabilized zirconia (YSZ) *J. Electrochem. Soc.* **164** F790–803
[35] Kilner J A 2000 Fast oxygen transport in acceptor doped oxides *Solid State Ion.* **129** 13–23

[36] Minervini L, Zacate M O and Grimes R W 1999 Defect cluster formation in M_2O_3-doped CeO_2 *Solid State Ion.* **116** 339–49

[37] Butler V, Catlow C R A, Fender B E F and Harding J H 1983 Dopant ion radius and ionic conductivity in cerium dioxide *Solid State Ion.* **8** 109–13

[38] Coduri M, Scavini M, Allieta M, Brunelli M and Ferrero C 2013 Defect structure of Y-doped ceria on different length scales *Chem. Mater.* **25** 4278–89

[39] Ou D R, Mori T, Ye F, Takahashi M, Zou J and Drennan J 2006 Microstructures and electrolytic properties of yttrium-doped ceria electrolytes: dopant concentration and grain size dependences *Acta Mater.* **54** 3737–46

[40] Li Z P, Mori T, Ye F, Ou D R, Zou J and Drennan J 2011 Structural phase transformation through defect cluster growth in Gd-doped ceria *Phys. Rev.* B **84** 1–5

[41] Coduri M, Checchia S, Longhi M, Ceresoli D and Scavini M 2018 Rare earth doped ceria: the complex connection between structure and properties *Front. Chem.* **6** 1–23

[42] Małecka M A, Burkhardt U, Kaczorowski D, Schmidt M P, Goran D and Kępiński L 2009 Structure and phase stability of nanocrystalline $Ce_{1-x}Ln_xO_{2-x/2-\delta}$ (Ln = Yb, Lu) in oxidizing and reducing atmosphere *J. Nanopart. Res.* **11** 2113–24

[43] Artini C, Costa G A, Pani M, Lausi A and Plaisier J 2012 Structural characterization of the CeO_2/Gd_2O_3 mixed system by synchrotron x-ray diffraction *J. Solid State Chem.* **190** 24–28

[44] Subramanian M A, Aravamudan G and Subba Rao G V 1983 Oxide pyrochlores—a review *Prog. Solid State Chem.* **15** 55–143

[45] Xu H and Wang Y 1999 Electron energy-loss spectroscopy (EELS) study of oxidation states of Ce and U in pyrochlore and uraninite—natural analogues for Pu- and U-bearing waste forms *J. Nucl. Mater.* **265** 117–23

[46] Garvie L A J and Buseck P R 1999 Determination of Ce^{4+}/Ce^{3+} in electron-beam-damaged CeO_2 by electron energy-loss spectroscopy *J. Phys. Chem. Solids* **60** 1943–7

[47] Bentley J, Gilliss S R, Carter C B, Al-Sharab J F, Cosandey F, Anderson I M and Kotula P J 2006 Nanoscale EELS analysis of oxides: composition mapping, valence determination and beam damage *J. Phys.: Conf. Ser.* **26** 69

[48] Sugar J, Brewer W D, Kalkowski G, Kaindl G and Paparazzo E 1985 Photoabsorption by the 3d shell in Ce, Pr, Ho, and Er: observations and calculations *Phys. Rev.* A **32** 2242–8

[49] Fortner J A and Buck E C 1996 The chemistry of the light rare-earth elements as determined by electron energy loss spectroscopy *Appl. Phys. Lett.* **68** 3817–9

[50] Alaydrus M, Sakaue M, Linh N H, Aspera S M, Wungu T D K and Kasai H 2015 Praseodymium doped ceria: the role of 4f-electrons of Pr dopant in doped ceria *ECS Trans.* **68** 369–73

[51] McNealy B E and Hertz J L 2014 On the use of the constant phase element to understand variation in grain boundary properties *Solid State Ion.* **256** 52–60

[52] Fleig J 2002 The grain boundary impedance of random microstructures: numerical simulations and implications for the analysis of experimental data *Solid State Ion.* **150** 181–93

[53] Gregori G, Merkle R and Maier J 2017 Ion conduction and redistribution at grain boundaries in oxide systems *Prog. Mater. Sci.* **89** 252–305